Beam shaping in light-sheet microscopy: an experimental analysis

Journal of Physics: Photonics

PAPER

Beam shaping in light-sheet microscopy: an experimental analysis

Manuel Hüpfel[1] and Gerd Ulrich Nienhaus[1,2,3,4,*]

[1] Institute of Applied Physics, Karlsruhe Institute of Technology (KIT), Wolfgang-Gaede-Str. 1, 76131 Karlsruhe, Germany
[2] Institute of Biological and Chemical Systems (IBCS), Karlsruhe Institute of Technology (KIT), 76021 Eggenstein-Leopoldshafen, Germany
[3] Institute of Nanotechnology, Karlsruhe Institute of Technology (KIT), 76021 Eggenstein-Leopoldshafen, Germany
[4] Department of Physics, University of Illinois at Urbana-Champaign, Urbana, IL 61801, United States of America
* Author to whom any correspondence should be addressed.

E-mail: uli@uiuc.edu

Keywords: light-sheet microscopy, beam shaping, fluorescence microscopy

Supplementary material for this article is available online

OPEN ACCESS

RECEIVED
26 December 2023

REVISED
18 April 2024

ACCEPTED FOR PUBLICATION
1 May 2024

PUBLISHED
13 May 2024

Abstract

Thanks to its unique optical sectioning capability, light-sheet fluorescence microscopy has proven to be a powerful technique for volumetric imaging of entire model organisms with high spatial and temporal resolution. For light sheet generation with scanned laser beams, holographic beam shaping offers precise control over the optical fields exciting the fluorescence. Various illumination schemes have been proposed, aiming for best image quality with regard to axial resolution, optical sectioning, illumination homogeneity and photobleaching while at the same time retaining a large field of view. Here, we have engineered and characterized a variety of beams and analyzed their imaging performance by using phantom samples and zebrafish embryos. These data may assist researchers to select the light sheet best suited to the imaging application at hand.

1. Introduction

In recent years, light-sheet fluorescence microscopy (LSFM) has attracted enormous attention in the biosciences, since it allows for fast volumetric imaging of cells and whole organisms with minimal phototoxicity and photobleaching [1–3]. In this modality, specimens are illuminated in sheets perpendicular to the optical axis of detection, and three-dimensional (3D) images are rapidly acquired by stepping the light sheet through the specimen, and taking a two-dimensional (2D) widefield image with a fast and sensitive scientific camera at each position.

The key advantage of LSFM over other fluorescence imaging modalities is its optical sectioning capability. With light sheet illumination, fluorophore excitation outside the focal plane of the detection objective is minimized, and so are out-of-focus background excitation and the ensuing photo-induced sample deterioration effects. The axial image resolution can be significantly enhanced by engineering the light sheet to be as thin as possible, whereas the lateral image resolution is solely governed by the numerical aperture (NA) of the detection objective. Light sheets can be formed either statically, e.g. by using a cylindrical lens to focus the light into a plane perpendicular to the propagation axis, or dynamically, by time modulating the illumination patterns during image capture [4, 5]. In digitally scanned light sheet microscopy (DSLM), a laser beam is swept sideways through the specimen to homogeneously illuminate a single plane [2]. When using a Gaussian beam (TEM_{00}) for this purpose, the light sheet is thinnest at the focus position and expands with distance from the focus due to diffraction. Consequently, both thickness and intensity vary across the light sheet. The focal radius, w_0, of the Gaussian beam is connected to the confocal parameter, i.e. the distance over which the beam radius is $<2^{1/2}\ w_0$, which can serve to define the usable range along the beam propagation axis [1, 4, 5]. When focusing the beam more tightly to create a thinner light sheet, the usable length inevitably decreases. Aiming to overcome this dilemma, a variety of sophisticated beams have been proposed [3, 6–9]. Most exciting are Bessel, Airy or Mathieu beams, which are solutions of the Helmholtz equation representing optical fields with propagation-invariant transverse intensity distributions [10, 11].

For these non-diffracting modes, finite-aperture approximations exist that maintain propagation invariance over a specific distance, making them suitable as light sheets for DSLM [10, 12]. Furthermore, these beams have a significant transverse wave vector component and self-reconstruct behind an obstacle, as unblocked parts of the optical field continue to converge behind the object and thus restore the central beam after the healing distance [13]. On the downside, non-diffracting beams are always accompanied by side maxima in the transverse plane. The zeroth-order Bessel beam has become most widely used in DSLM and many other applications [12, 14]. Its sharp central maximum is ideal for generating a thin light sheet, yet it is enwrapped in coaxial intensity rings associated with the side maxima of the Bessel function, J_0, carrying a substantial fraction of the total energy. These light structures excite substantial out-of-focus fluorescence, impairing image contrast as well as resolution. Fortunately, such background can be effectively suppressed with confocal slit detection (CSD) [15]. In this camera mode, a rolling shutter is synchronized with the sweeping beam forming the light sheet to capture the image as a sequence of narrow strips. There are various other techniques aimed at optimizing DSLM light sheets, for which we refer to a recent review [16]. Furthermore, the raw image data can be honed by image processing, including multi-view deconvolution [17–19], structured illumination microscopy [20] or background correction algorithms [21].

The abundance of DSLM beams calls for a thorough analysis of their properties and imaging performances, to enable an informed selection for the imaging problem at hand. Recent insightful studies aiming at systematic comparisons covered only a small subset of light beams [22–24] or relied heavily on computation [8]. Here we have pursued a broader experimental analysis, focusing on DSLM with a large field of view (FOV) of several hundred microns, as appropriate for the study of developing model organisms. We engineered a set of nine different scanned light sheets by holographic shaping of a Gaussian laser beam, all of which could be created with high power throughput, as fast imaging of large specimens calls for high excitation power. After thorough optical characterization of the beams, we quantitatively assessed their imaging properties with fluorescent 100 nm nanobeads immobilized in a gel matrix. Furthermore, we imaged a zebrafish embryo with fluorescently labeled cell nuclei, visible as puncta of ∼5 μm in diameter. At 12 h post fertilization (hpf), they display strongly scattering and absorbing cell clusters at the head and tail buds [25]. We hope that the data presented here will give guidance to researchers in the selection of beams that are best suited for their specific DSLM application.

2. Methods

2.1. DSLM setup

A schematic of our custom-built DSLM, modified from the previously described setup [21], is depicted in figure S1. All measurements were carried out with one-sided illumination by 561 nm laser light, focused into the specimen with a dry objective (CFI LU PlanFluor 5×/0.15 A, Nikon GmbH, Düsseldorf, Germany) (figure 1(a)). The fluorescence emission was collected with a water immersion objective (CFI-75 LWD 16×/0.8 w, Nikon GmbH, Düsseldorf, Germany) and imaged onto an sCMOS camera (ORCAFlash 4.0 V2, C11440-22CU, Hamamatsu Photonics K.K., Hamamatsu, Japan) with a 2048 × 2048 pixel sensor. The FOV covers 825 × 825 μm^2; no pixel binning was used to ensure the highest possible sampling frequency. In rolling shutter mode, only a limited number of adjacent pixel lines of the sCMOS camera are activated at a time. For CSD, this active strip (here, 8.3 μm wide) was synchronized with the illumination beam scan [15]. A dark image, measured beforehand, was subtracted from each frame of the image stack immediately after acquisition to remove camera noise.

2.2. DSLM beam selection and generation

DSLM beams were generated with a reflective, phase-only spatial light modulator (SLM, LETO, Holoeye Photonics AG, Berlin, Germany), featuring a liquid crystal on silicon display with 1920 × 1080 pixels (active area 12.5 × 7.1 mm^2) and a pixel size of 6.4 μm. Each pixel was loaded with a phase value according to a specifically designed pattern, which was calculated beforehand with the help of a MATLAB script that is freely available via GitHub (https://github.com/NienhausLabKIT/HuepfelM). For inspection of the intensity distributions at the focus position of the beams, a flip mirror was positioned in the beam path after the SLM (figure S1) to allow for redirection of the light path towards a camera (DCC1545M, Thorlabs).

In this work, we included the Gaussian beam for reference, three double beams, a C-beam, sectioned Bessel beams and, for the first time, sectioned droplet beams (figures 1(b)–(f)). All beams had to meet two specific requirements. Firstly, since we focus on DSLM for organismal imaging, we considered only beams with large and similar propagation lengths (∼360 μm, figure 1(d)). Notably, propagation length, main-lobe width and the spatial dispersion of the intensity are mutually interdependent, and, therefore, a fair

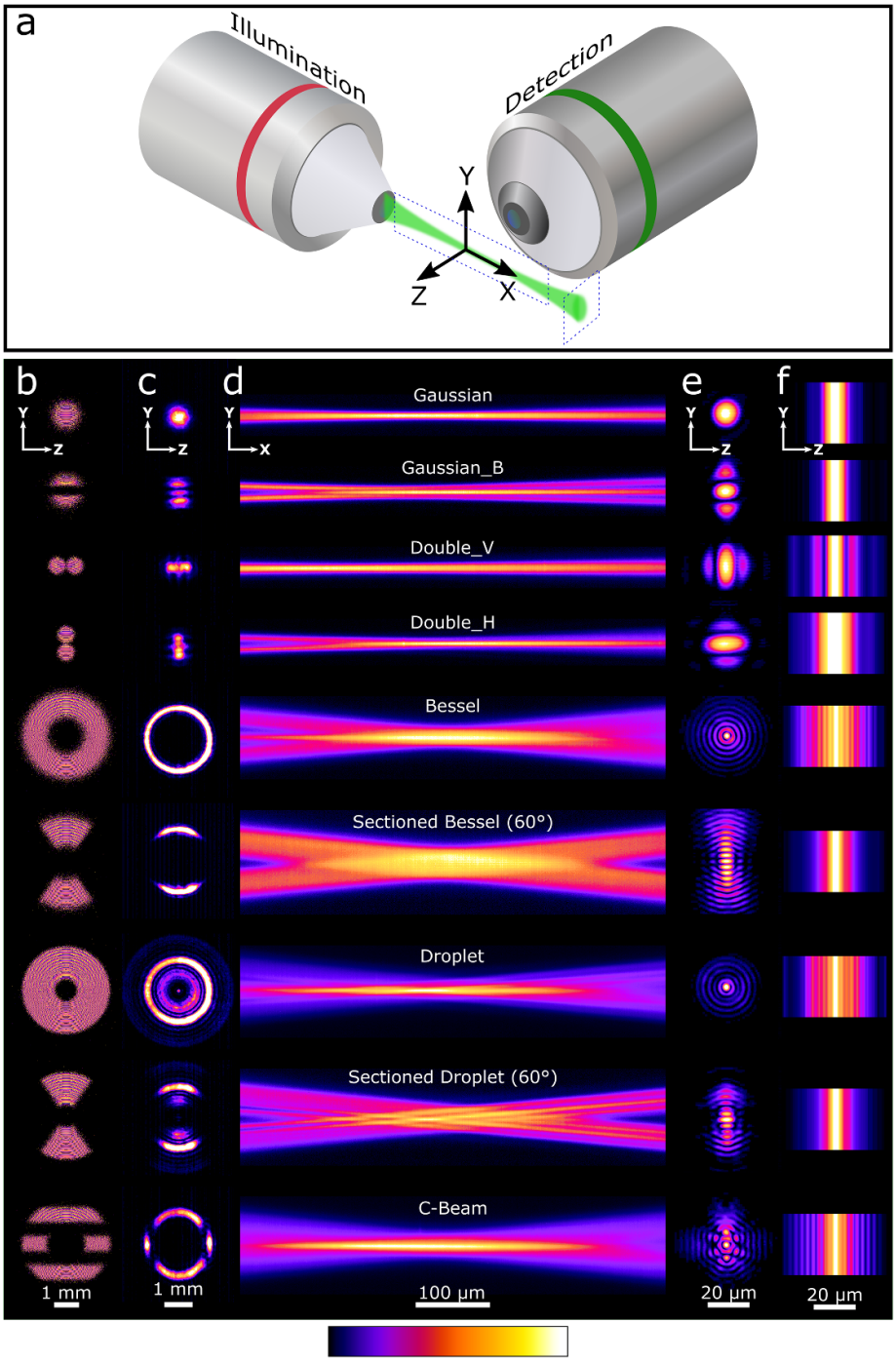

Figure 1. Coordinate system and overview of the DSLM beams and the resulting light sheets selected for this study. (a) Arrangement of illumination and detection objectives and coordinate system definition (light propagating along *x*, beam scanned along *y*, detection axis along *z*). (b) SLM phase patterns for beam shaping. (c) Intensity distribution in the back focal plane of the illumination objective, measured by mounting an inspection camera in front of the back aperture of the illumination objective. (d) Cross sections of the beams in the *xy*-plane (light sheet plane), measured via light scattering by water in the sample chamber with the microscope camera. (e) Cross-sectional intensity at the focus position, measured with the (confocally positioned) inspection camera setup near the SLM (unit A in figure S1). (f) Time-averaged intensity distribution of the scanned beam, created by shifting and integrating the cross sections in panel (e) along the *y*-direction to emulate beam scanning.

comparison requires comparable propagation lengths. A second constraint is imposed by the need for a large power throughput in the holographic beam shaping procedure to ensure a good signal-to-noise ratio across the large FOV. Thus, holographic patterns that require masking of large area fractions on the SLM, e.g. lattice light beams [3], were excluded here. The holographic patterns of the nine beams are described in the supplementary materials and are depicted in figure 1(b) (see also figure S2 for an expanded view).

2.3. Zebrafish embryo preparation and imaging

Zebrafish housing and husbandry were performed as recommended [26]. To image zebrafish embryos featuring fluorescent cell nuclei, embryos of the transgenic line *Tg(h2az2a:h2az2a-mCherry)* were fixed at 12 hpf using 4% paraformaldehyde. Subsequently, they were immunolabeled [27] first with anti-RFP primary IgG antibodies, which bind to the red fluorescent mCherry protein [28] fused to the nuclear (chromatin) protein histone 2a, and then with Alexa Fluor 561-labeled secondary IgGs. Finally, the embryos were gently pipetted into 1.5% low melting point agarose solution (type VII, A6560, Sigma Aldrich, St. Louis, MO) at 38 °C. Part of the solution was loaded into a fluorinated ethylene propylene (FEP) tube (inner diameter 2.34 mm, wall thickness 0.23 mm, Reichelt Chemietechnik GmbH, Heidelberg, Germany) with a syringe. After gelling, the tube containing a single immobilized embryo was mounted in the sample chamber of the microscope by attaching it to a steel rod and inserting it into the rotation stage.

With these samples, we acquired stacks of 300 frames (spacing 1 μm) at a beam power of 200 μW. Without CSD (global shutter), the exposure time per frame was set to 200 ms; with CSD (rolling shutter), the exposure time per frame was 100 ms and the line exposure time was 1 ms.

2.4. Bead phantom preparation and imaging

An imaging phantom was prepared inside a FEP tube (same type as above), consisting of fluorescent polystyrene nanobeads (F8801, FluoSpheres, Invitrogen, Eugene, OR, excitation/emission peak wavelengths 580/605 nm, diameter 100 nm) immobilized in a 1.5% (by mass) agarose gel, as described earlier [21]. Before mounting, the gel was gently extruded from the FEP tube to avoid optical aberrations by the tube. However, aberrations (mainly astigmatism) arising from the slight refractive index mismatch between the agarose cylinder and the aqueous surroundings cannot be ruled out.

With the nanobead sample, we acquired image stacks of 300 frames (1 μm spacing) with and without CSD at a beam power of 440 μW. The frame exposure time was 200 ms; for CSD, the line exposure time was set to 2 ms. We note that with a slit width of 8.3 μm, the full range (825 μm) is covered by ∼100 lines, yielding an effective frame exposure time of ∼200 ms.

In the image analysis, we first subtracted the camera offset from the bead images. In the next step, a maximum intensity projection was computed, and the positions (x- and y-coordinates) of local maxima were determined within the propagation range of the beams. For each maximum, we plotted the intensity profile along the axial direction (z-axis, figure 2(a)), and fitted a Gaussian to extract the amplitude and FWHM. Finally, we averaged the amplitudes and FWHM values of all beads (between 100 and 250 depending on the beam used).

2.5. Image analysis

Images were processed automatically within Fiji/ImageJ [29] using macros written for this purpose, which have been made freely available via GitHub (https://github.com/NienhausLabKIT/HuepfelM).

2.6. Numerical calculation of beam propagation

We calculated the intensity distribution generated by our phase patterns with the numerical wave propagation plugin in ImageJ using the angular spectrum method [30, 31]. By calculating the cross-sectional intensity from 0–500 μm in 2 μm steps along the propagation direction, we characterized the beam profile (and other parameters) in the entire range of interest, including locations difficult to access experimentally.

3. Results

3.1. Light sheet characterization

Owing to its simplicity, the Gaussian beam is most commonly used in DSLM and serves as a reference here. Its beam diameter varies along the propagation axis due to diffraction, affecting both thickness and intensity of the resulting light sheet (figure 1(d)). As the intensity is concentrated along the propagation axis, pronounced stripe artifacts appear in the image behind strongly absorbing or scattering obstacles [32]. We have further investigated three beams formed by two 'sub-beams' propagating at an angle relative to the optical axis, generating typical two-beam interference fringes in the focal region. One of them, here referred to as 'Gaussian blocked' (Gaussian_B), is made by simply blocking a central strip on the phase mask of the Gaussian beam (figure 1(b)), as was reported earlier [9]. By contrast, the 'Double beam' [8] uses circular apertures on the phase mask to generate the two sub-beams. Here we have studied two variants, denoted Double_V (for vertical) and Double_H (for horizontal), which differ in the orientation of the two apertures and thus display their fringe pattern along the z-axis (detection axis, figure 1(a)) and y-axis (beam scanning axis), respectively. Note their markedly different time-averaged light pattern upon beam scanning to create

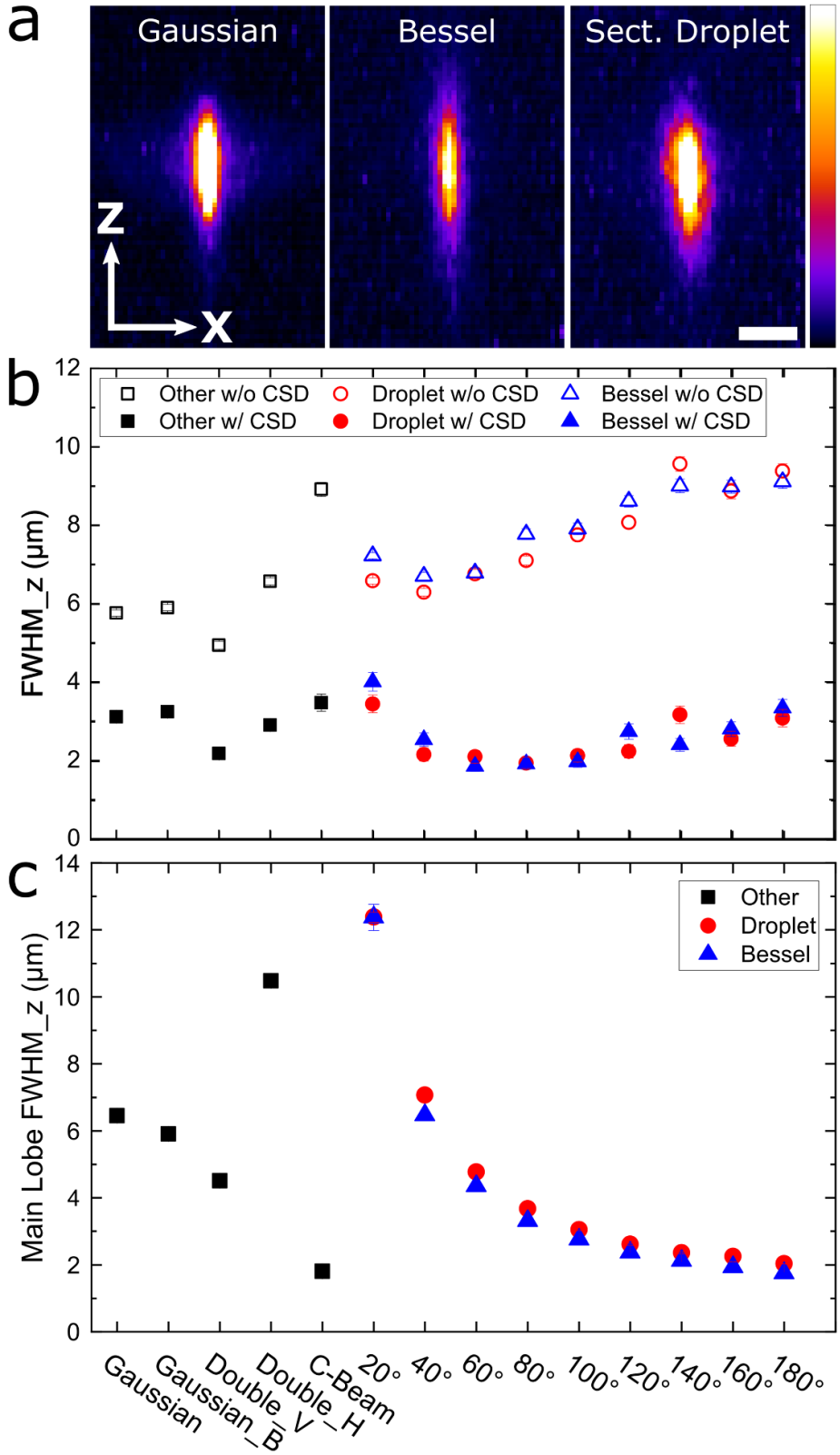

Figure 2. Axial image resolution and main lobe thickness of the different beams generating the scanned light sheet. (a) Exemplary *xz*-sections of PSFs acquired with Gaussian, Bessel and sectioned Droplet illumination of 100 nm fluorescent beads (without CSD). Scale bar, 5 μm. (b) Plot of the FWHM_z, quantifying the apparent extension along the axial direction of the bead images, taken with and without CSD. Data show mean and standard error of the mean, determined from Gaussian fits to the central PSF sections of typically 100–250 beads. (c) Plot of the main lobe FWHM_z, quantifying the axial extension of the different beams. Data show mean and standard error of the mean, determined from Gaussian fits to cross-sectional images at the focus positions, averaged over three independent measurements.

Table 1. Parameters of the DSLM beams from fits to the measured intensity distributions.

Beam	Length (μm)[a]	Main lobe FWHM_z (μm)[b]	SD w/o CSD (μm)[c]
Gaussian	358.9 ± 2.2	6.45 ± 0.02	2.570 ± 0.003
Gaussian_B	386.3 ± 4.2	5.91 ± 0.01	2.355 ± 0.003
Double_V	374.1 ± 3.5	4.51 ± 0.01	3.469 ± 0.003
Double_H	373.8 ± 3.5	10.48 ± 0.03	4.151 ± 0.003
Bessel	356.9 ± 1.0	1.75 ± 0.02	5.768 ± 0.005
Sect. Bessel	364.6 ± 2.3	4.35 ± 0.04	3.359 ± 0.005
Droplet	339.7 ± 1.2	2.03 ± 0.01	4.922 ± 0.005
Sect. Droplet	335.6 ± 3.3	4.77 ± 0.06	2.738 ± 0.005
C-Beam	328.2 ± 1.0	1.81 ± 0.01	5.403 ± 0.003

[a] quantified as the width (FWHM) of the intensity distribution along the beam propagation axis.
[b] width (FWHM) of the main lobe intensity distribution along the detection axis, as shown in figure 2(c).
[c] standard deviation of the axial intensity distribution of the scanned light sheet along the detection axis, as shown in figure 3(c).

the light sheet (figure 1(f)). Unlike Double_H, which generates a broad scanned light sheet, Double_V has a thin main light sheet and axially displaced satellite sheets. In addition, we have included the Bessel beam for its beneficial non-diffracting and self-healing properties, allowing for deeper sample penetration and better homogeneity of illumination. However, with its concentric ring system around the sharp central beam carrying a large fraction of the overall power, it generates significant background due to excitation of fluorescence outside the focal plane [12, 33]. Sectioned Bessel beams were introduced to mitigate this effect while (partly) retaining self-healing properties, improving optical sectioning capabilities and FOV [7]. We have studied their behavior over the entire range of sector angles (in 20° steps), extending from a two-beam interference field at small angles, with fringes in the light sheet plane, to the complete coaxial Bessel optical field. Another interesting approach to suppressing Bessel beam fringes is through interference of two or more concentric Bessel beam systems with suitably chosen transverse wave vectors, which results in a beam with multiple intensity maxima along the propagation axis resembling water droplets [6, 34]. Thus, we included a 'droplet beam' in our comparison and, furthermore, investigated if further reduction of axial field components by sectioning of the droplet beam is beneficial for DSLM. We have not considered lattice light sheets [3], as they are associated with high energy losses [5], limiting their use to small-FOV applications [35]. Instead, we have included the recently introduced 'C-beam', resembling a lattice light sheet but using wider apertures [36].

All nine holographically shaped beams were engineered to have comparable propagation lengths. These were quantified by fitting Gaussians to a 4 μm wide slab of the intensity distribution in the *xy*-plane along the propagation axis (figure 1(d)). This simple heuristic approach works very well for these beams. The lengths are compiled in table 1 as average FWHM values of the fitted Gaussians and their standard errors from three independent measurements.

3.2. Axial resolution

A thinner light sheet can significantly improve the axial resolution, since the effective point spread function (PSF, i.e. the image of a 0D object) of the system is the product of the relevant spatial distributions associated with the excitation and detection paths. To examine the widths of our beams, we collected volumetric images of our phantom sample containing 100 nm fluorescent beads immobilized in agarose gel, both with and without CSD. Notably, since the *z*-axis extension of the excitation PSF is on the micron scale for all beams, the broadening effect due to the intrinsic size of the beads is negligible. Figure 2(a) shows exemplary bead images (*xz*-sections) taken with different beams (without CSD). To determine the average width along the axial (*z*) direction (figure 1(a)), we located individual beads (100–250 depending on the beam type) in the 3D stacks, extracted their axial intensity profiles, and fitted them with Gaussian functions to obtain the FWHM_z values plotted in figure 2(b).

The axial bead profile measured with the Gaussian light sheet reveals a FWHM_z value of 5.8 μm (figure 2(b)). For the two-beam patterns, there are slight variations, in line with the variations in the intensity distributions (figures 1(e) and (f)). For instance, the Double_V beam has minimal axial width due to its narrow central lobe and its well-separated side lobes (figure 1(e)), whereas the Double_H beam has an axially elongated PSF (figure 1(e)) due to its narrow frequency spectrum along the *z*-axis (figure 1(c)). For the same reason, sectioned Bessel and droplet beams with small sector angles ($<60°$) have a comparable FWHM_z. It increases monotonically with sectioning angle $\geqslant 40°$ up to $\sim$9 μm, as the optical field broadens along the *z*-direction until it finally forms the full coaxial ring system (figure 1(e)) creating strong tails along

z when the beam is scanned (figure 1(f)). Notably, there are only minor differences in the FWHM_z parameter between Bessel and droplet beams despite the effective side lobe suppression of the latter, which is clearly visible in figure 1(e). This is a consequence of the broader main maximum of the droplet beam due to its less sharply focused inner Bessel system. Not surprisingly, the C-beam has about the same FWHM_z value as the Bessel or droplet beams, in line with its similar frequency distribution (figure 1(c)).

CSD suppresses intensity laterally, i.e. in the image plane along the scanning axis (y), as well as axially (z) via the confocal effect. As a result, the axial resolution is significantly enhanced for all beams (figure 2(b)). For the Gaussian and the two-beam fields, FWHM_z is smaller by ∼3 μm with CSD, as compared to global shutter image acquisition. For the sectioned Bessel and droplet beams, the sector angle increasing from small values causes a sharpening of the central peak, leading to a minimal FWHM_z of ∼2 μm at ∼80°. For greater angles, FWHM_z increases again due to the continuous strengthening of the side maxima along z.

The FWHM_z values without CSD in figure 2(b) are significantly larger than the axial resolution estimated to be 2.5 μm (using $2\lambda n/\mathrm{NA}^2$, with wavelength, $\lambda = 605$ nm, index of refraction, $n = 1.33$, and numerical aperture, $\mathrm{NA} = 0.8$) for our high-NA objective, but are in line with data reported for the same objective [37, 38]. The relatively coarse sampling (403 nm laterally and 1 μm axially) is a resolution-limiting factor, and there are also sample-induced aberrations. Importantly, the agarose cylinder has a refractive index slightly different from the aqueous environment and thus introduces astigmatism.

It is instructive to compare the bead image (axial resolution) data in figure 2(b) with the extension of the main lobe of the different beams in the axial direction (figure 2(c)), which we measured at the focus positions (figure 1(e)) and quantified with Gaussian fits; numerical data are included in table 1. For the Gaussian and the two-beam fields, the main lobe widths vary roughly as expected from the FWHM_z values of the beads. Notably, the Double_H beam, which is axially poorly confined (figure 1(e)), is more extended than determined from the bead image FWHM_z due to the confining effect of the detection PSF in the bead image. Even greater is the main lobe axial extension for the 20°-sectioned Bessel beam, reflecting its narrow frequency spectrum along the z-direction. With increasing sector angle, the main lobe sharpens continuously and reaches ∼1.75 μm at 180°. The droplet beam is axially slightly wider at all angles than the Bessel beam due to the lower frequencies associated with the inner ring system. From comparing the data in figures 2(b) and (c), it is obvious that the axial resolution severely suffers due to the Bessel ring systems unless we suppress them by using CSD. In our DSLM setup, designed for organismal imaging with large FOV (low NA illumination), excellent axial resolution is achieved with sectioned Bessel beams at intermediate sector angles, which establish a good balance between main lobe sharpening and side lobe suppression.

3.3. Image contrast

In organismal imaging, specimens typically exhibit strong and spatially varying scattering and/or absorption, causing the image quality to deteriorate, as the signal-to-background ratio decreases and imaging artifacts appear. To examine our light sheets in a realistic setting, we collected 3D stacks of zebrafish embryos with and without CSD under otherwise identical conditions. Exemplary images taken with CSD are shown in figure 3(a); the complete set has been included in the supplementary materials (figures S3 and S4). Some differences upon varying the imaging conditions are quite apparent, such as the enhanced contrast with CSD (figures S3 and S4) [15], or the suppression of stripe artifacts (figure 3(a)) with Bessel or sectioned droplet illumination [32, 39]. Furthermore, close inspection reveals variations in the detailed spot patterns visualized with the different beams (figure 3(a)).

Image contrast is an essential quality parameter, and for comparison of our illumination beams, we have generated a contrast metric in the following way. All images were normalized to the mean intensity of the reference (i.e. the Gaussian beam with CSD), and the standard deviation was calculated within a selected region of interest for 20 consecutive frames of each image stack. In figure 3(b), we have plotted the mean of these 20 values as a measure of contrast. Without CSD, the highest contrast is achieved with Gaussian and Gaussian_B beams, as they are well confined along the z-axis (figures 1(e) and (f)) and excite fluorescence predominantly in the focal plane of the detection objective. The Double_V and Double_H beams are somewhat more dispersed along the z-axis due to side maxima and main lobe broadening, respectively, and so provide lower contrast due to more out-of-focus fluorescence excitation. For the sectioned Bessel and droplet beams, contrast deteriorates with increasing sector angle, as the intensity spreads more and more along the z-dimension. By the same token, the C-beam yields contrast similar to the complete Bessel and droplet beams.

CSD effectively suppresses out-of-focus fluorescence and so greatly improves contrast for all beams (figure 3(b)). Quantitatively, the effect varies between the beams. Notably, the Gaussian beam provides the highest contrast, followed by the two-beam patterns and the sectioned Bessel or sectioned droplet beams with sectioning angles between 60° and 80°, which all give similar contrast (figure 3(b)). The slightly better contrast of the sectioned droplet beams in comparison to the corresponding Bessel beams for sector angles

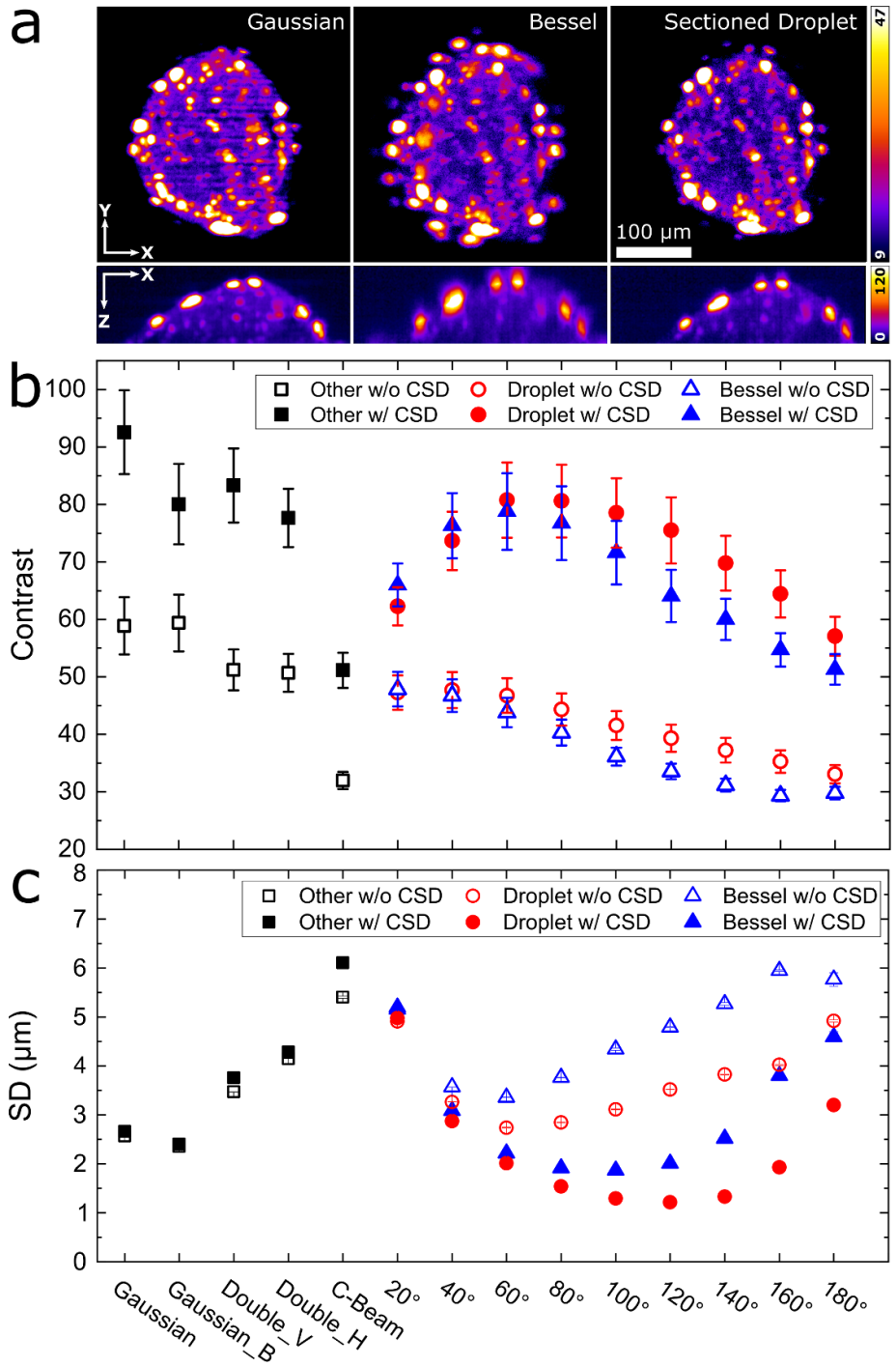

Figure 3. (a) Single slices from a 3D stack showing cell nuclei of a zebrafish embryo illuminated with Gaussian, Bessel and sectioned droplet (60°) beams and using CSD. (b) Mean image contrast and standard error of the mean from 20 images of a zebrafish embryo, taken with and without CSD. For all beams, contrast was quantified by calculating the standard deviation from the mean image intensity (normalized to unity) within a representative image region. (c) Standard deviation of the z-axis intensity distribution at the beam focus, calculated by integrating the intensity in the yz-image (figure 1(e)) over the entire scan range (without CSD) or over a central strip (with CSD). Data have been scaled to object coordinates.

>60° is in line with its suppressed side lobes. The extent of contrast improvement with CSD depends on the structure of the optical field. For example, CSD strongly suppresses out-of-focus fluorescence excited by the well-separated side lobes of the Double_V beam. As we may expect, it is somewhat less effective in reducing fluorescence excited by the axially extended main lobe of Double_H (figures 1(e) and (f)). For the sectioned Bessel and droplet beams, the effectiveness of CSD first improves with increasing sector angle (figure 3(b)), as the light becomes more concentrated along the *z*-axis, and CSD ensures suppression of the side maxima in the focal *yz*-plane (figure 1(e)), which become successively broader along the axial direction with increasing

index. At larger angles, this trend reverses as the side lobe pattern gains strength along the axial direction even for $y \approx 0$ (figure 1(e)).

The data in figure 3(b) emphasize the crucial role that the spatial confinement of the excitation beam along the axial direction plays for achieving good image contrast, as has been stressed before [8, 22]. Ideally, the optical field should transport all power within the focal depth of the detection objective, as light outside this zone excites only background fluorescence. To connect the imaging contrast (figure 3(b)) to intrinsic beam properties, we have analyzed the axial intensity distributions of our light sheets. Oftentimes, the axial distribution is quantified by the range containing 63% of the beam power [23], although such an arbitrary cutoff cannot capture the full nature of the complicated spatial intensity distributions. Here we have chosen an alternative approach and calculate the standard deviation, i.e. the square root of the second central moment of our intensity distributions along the axial direction,

$$\mathrm{SD} = \sqrt{\frac{\sum_{i=1}^{n} I(z_i)\,[z_i - \bar{z}]^2}{\sum_{i=1}^{n} I(z_i)}}, \tag{1}$$

with $I(z_i)$ and $\bar{z}$ denoting the axial intensity distribution along the z-axis and its center position (first moment of the distribution), respectively.

We determine the SD from the intensity pattern in the yz-plane (figure 1(e)), either by integrating the full pattern along the y-axis to represent image acquisition without CSD, or only over the slit width chosen for CSD, as illustrated in figure S5(a). Note that we only capture the lateral but not the axial confocal confinement effect in this calculation. Therefore, the data in figure 3(c) fail to display the expected CSD-induced reduction in the axial extension for those beams that are significantly distributed along the z-coordinate (e.g. Gaussian, Gaussian_B, Double and C-beam). Numerical data are included in table 1.

Without CSD, the 'Gaussian_B' beam features the highest spatial confinement of the excitation intensity; better optical sectioning can only be achieved with sectioned Bessel or droplet beams at intermediate sector angles using CSD (figure 3(c)). For the latter beams, the SD plot faithfully reproduces the enhanced axial confinement due to suppression of the lateral side maxima in the yz-plane, which are axially more extended (figures 1(e) and S5). For the sectioned Bessel beams, our experimental data agree well with simulations for both detection modes (with and without CSD) [7]. Furthermore, SD is consistently smaller for sectioned droplet beams than for their Bessel counterparts due to side lobe suppression of the droplet pattern [6], both with and without CSD. The variation of SD with sector angle is roughly inverse to the one of the image contrast (figure 3(b)). Thus, high contrast coincides with small SD, which underscores the key role of axial confinement of the excitation pattern for image contrast. As the experimental SD data are solely based on the intensity distributions at the focus, we have additionally performed simulations in 2 μm steps in the range between -50 μm and $+50$ μm (figure S5(b)). The averages are qualitatively in line with the analysis at the focus, and the variations along the propagation (x) direction are visible through the error bars.

3.4. Power efficiency

In fluorescence microscopy, it is important to ensure that the photon flux impinging on the sample is optimally utilized for image formation, as the inevitable photobleaching of the fluorophores and phototoxicity (in live specimen imaging) are key factors limiting exposure times and, accordingly, the signal-to-noise ratio of the acquired images. Therefore, we have examined the power efficiency of our light sheets using the highly homogenous fluorescent nanobeads of the bead phantom sample as 'standard candles'. We have kept the laser power entering the illumination objective constant, so the integrated fluorescence intensity from the beads can be taken as a measure of the power efficiency of the different beams, representing the fraction of light that contributes to the image.

In figure 4(a), the integrated bead intensity, normalized to unity for the maximum value (i.e. for the Double_H beam), is plotted for all investigated light beams. Without CSD, it is largest for the Gaussian and two-beam fields (figure 4(a)); roughly half of the signal is rejected upon using CSD. The (sectioned) Bessel and droplet beams have a much lower efficiency of around 40% even without CSD. The effective suppression of out-of-focus background with CSD is reflected by a power efficiency of only ~10%. As suspected, the power efficiency is rather poor for these spread-out optical fields.

However, the integrated intensity does not convey the full story, as a sharply focused beam will concentrate more bead fluorescence into fewer voxels, which will gain appreciable amplitudes above background more quickly. Therefore, we have also calculated the normalized peak intensities of the Gaussians fitted to the bead images (figure 4(b)). Again, the highest amplitudes are observed for the Gaussian and the two-beam fields. For the sectioned Bessel and droplet beams, the peak intensity shows a

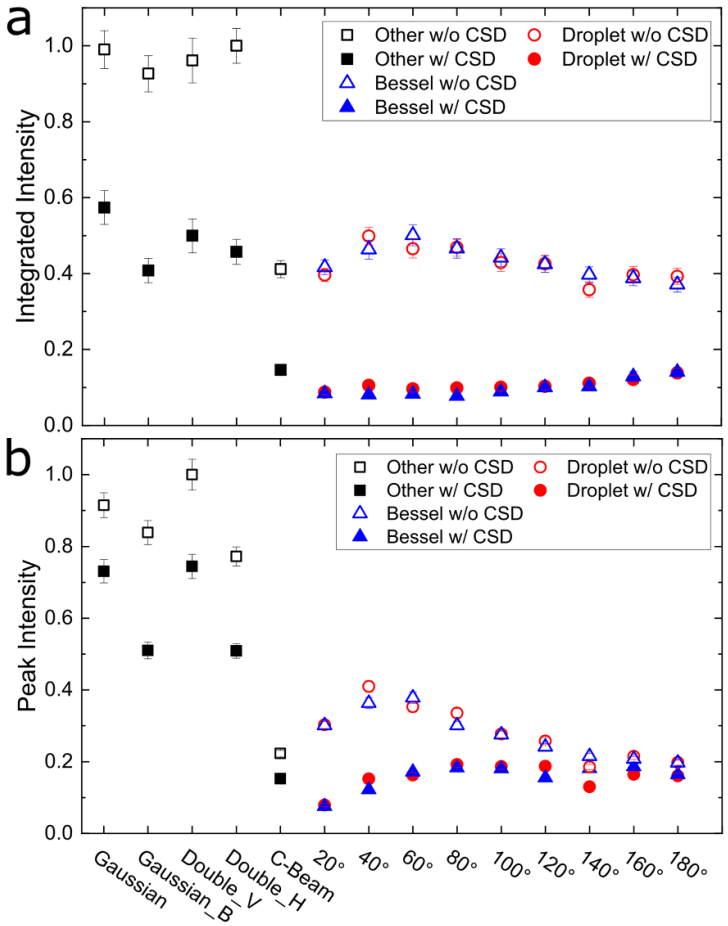

Figure 4. (a) Integrated intensity and (b) peak intensity of images of 100 nm latex beads exposed to the different beams with and without CSD. Data were extracted from Gaussian fits to the axial intensity distributions and, for easy comparison, normalized to unity for the largest values. Symbols: mean values over typically 100–250 beads, error bars: standard error of the mean.

systematic dependence. Without CSD, it increases to 40% at 40°–60° sector angle and then decreases again, whereas with CSD, there is a rise up to ∼20% at somewhat greater angle (60°–80°). This behavior correlates with the axial image resolution (figure 2(b)). Accordingly, the largest peak intensities are achieved at intermediate sector angles, where the axial resolution is best. Note that the integrated intensities are roughly constant (figure 4(a)). Taken together, the peak intensity of these beams is lower by more than a factor 3–4 than for the Gaussian and two-beam patterns, hampering their use with light-sensitive samples.

3.5. Self-healing capability

We have investigated self-healing of our beams behind a small scattering obstacle that was immobilized in a fluorescently stained agarose gel (figure 5(a)); close-ups are shown in figure 5(b). For the Gaussian beam, visual inspection shows prominent stripe artifacts behind the defect, as reported previously [32]. For the Gaussian_B and the two-beam patterns, the stripes appear slightly reduced. The artifacts are hardly visible for Bessel or droplet illumination due to their axial symmetry with respect to the propagation direction. For the sectioned variants, they become more pronounced with decreasing sector angle and, therefore, more restricted angular spectrum for beam reconstruction.

For quantification of the self-healing effect, we analyzed the intensity fluctuations in the line profile taken ∼100 μm behind the obstacle (green bar in figure 5(a)). To this end, we normalized the intensity to an average of one in the chosen range (figure 5(c)) and calculated the standard deviation for each profile (figure 5(d)). This analysis agrees well with the visual impression from the close-ups and shows the more effective suppression of fluctuations with increasing sector angle for the Bessel and droplet beams (figure 5(d)).

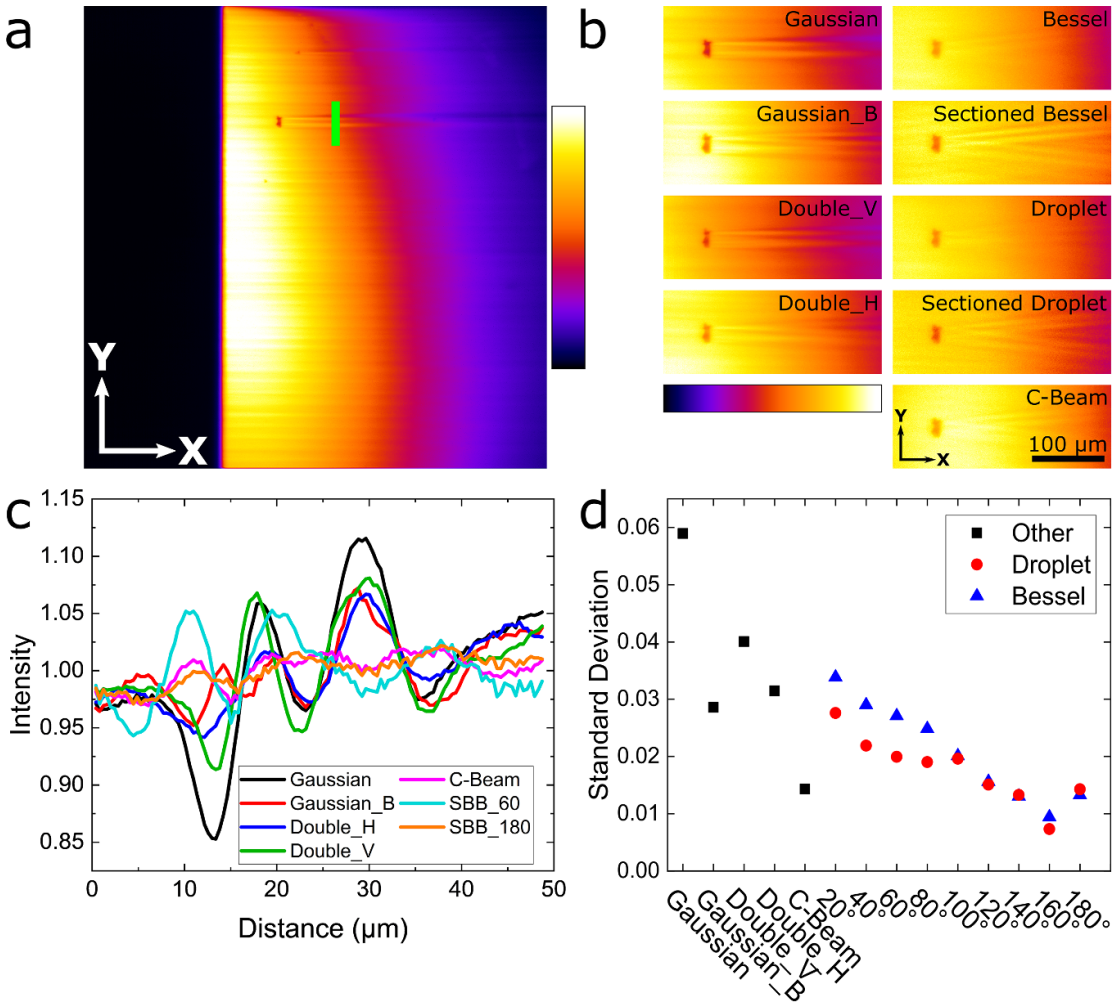

Figure 5. Stripe artifacts behind an obstacle generated by the different beams. (a) Image of an Alexa Fluor 568 dye-stained agarose gel, acquired by illumination with a Gaussian beam propagating along the *x*-axis and CSD. The optical density was ∼1 for a sample thickness of 400 μm. A scattering defect, visible in the upper part, gives rise to stripe artifacts. (b) Close-up images of the scattering defect in an agarose gel sample homogeneously stained with the Alexa Fluor 568 dye, taken with a power of 1.3 μW for all beams and CSD. (c) Intensity profiles along the *y*-axis (averaged over the *x*-range indicated by the thickness of the green bar in panel (a), normalized to their mean value for the different beams (colors assigned in the inset). The fluctuations represent the stripe artifacts generated by the different beams. (d) Quantification of the fluctuations through the standard deviation of the normalized line profiles in panel (c).

4. Discussion

In this study, we have examined a wide selection of beams for use in DSLM with a large FOV suitable for organismal imaging. This application requires illumination with low NA beams, yielding light sheets of a few micron thickness over the target propagation length of several hundred microns. Importantly, we have only examined beams that could be shaped holographically without substantial power loss. After thorough characterization of the different light patterns, we performed imaging experiments, always with and without CSD, on bead phantom and zebrafish embryo samples to extract the relevant parameters axial resolution, image contrast, power efficiency and stripe artifact generation. For a quick overview, table 2 provides a simple, qualitative summary of our results in the form of a five-star rating. In the following, we discuss the results and draw conclusions about the benefits of the different beams for DSLM.

The most commonly used Gaussian beam and, similarly, the two-beam patterns offer good resolution, contrast and power efficiency without CSD, which is a direct consequence of their good *z*-axis focusing (figure 3(c)). These beams are advantageous for imaging densely labeled samples, which inevitably suffer from out-of-focus fluorescence due to poor optical sectioning [8]. As expected, when using CSD, the power efficiency drops significantly, yet the effect is compensated by a substantially improved contrast. Altogether, these beams are clearly preferable for light-sensitive samples. The Gaussian beam shows strong stripe artifacts, however, which can be alleviated to a significant extent by using two-beam patterns (figure 5). There are other effective ways to deal with such artifacts, e.g. two-sided/bidirectional illumination, pivoting

Table 2. Imaging performance of the different beams for DSLM imaging with (★) and without (☆) CSD based on a five-star rating.

Beam type	Axial resolution	Image contrast	Power efficiency	Self-healing
Gaussian	☆☆ ★★★★	☆☆☆ ★★★★★	☆☆☆☆☆ ★★★★	☆ ★
Gaussian_B	☆☆ ★★★★	☆☆☆ ★★★★	☆☆☆☆☆ ★★★	☆☆ ★★
Double_V	☆☆☆ ★★★★	☆☆ ★★★★	☆☆☆☆☆ ★★★★	☆☆ ★★
Double_H	☆☆ ★★★★	☆☆ ★★★★	☆☆☆☆☆ ★★★	☆☆ ★★
Bessel	☆ ★★★★	☆ ★★★	☆☆☆ ★	☆☆☆☆☆ ★★★★★
Sect. Bessel (60°)	☆☆ ★★★★★	☆☆ ★★★★	☆☆☆☆ ★	☆☆☆ ★★★
Droplet	☆ ★★★★	☆ ★★★	☆☆☆ ★	☆☆☆☆☆ ★★★★★
Sect. Droplet (60°)	☆☆ ★★★★★	☆☆ ★★★★	☆☆☆☆ ★	☆☆☆ ★★★
C-Beam	☆ ★★★	☆ ★★★	☆☆☆ ★	☆☆☆☆☆ ★★★★★

the light sheet, multi-view imaging and post-processing techniques [16, 32]. Although substantial hardware efforts are involved, we typically employ two-sided illumination in our experiments.

If aiming for highest axial resolution, Bessel or droplet beams and their sectioned variants offer clear advantages, thanks to their sharp central maxima, but only in combination with CSD. We have seen best results with sectioned beams at intermediate sector angles, providing a balance between main lobe sharpening and overall spreading along the axial direction. These beams are comparable to the two-beam patterns in terms of contrast (figure 3(b)); the Gaussian beam is still somewhat superior, though. However, we stress that these beams have rather poor power efficiency (figure 4) and thus excite (predominantly!) out-of-focus fluorescence, which limits their application to samples that are more resistant to photodamage. Notably, multi-view imaging combined with image fusion is an excellent alternative in less time-critical applications, achieving even isotropic resolution [17, 19, 40].

Post-processing via image deconvolution is another valuable and widely used approach that can further enhance resolution by correctly reassigning out-of-focus fluorescence produced by side lobes [41]. However, deconvolution is an ill-posed mathematical operation and crucially relies on a precisely characterized PSF of the instrument. In organismal imaging, the intrinsic variations of the light sheet as well as index variations within the sample render the PSF spatially variant, adding extra complexity to the deconvolution problem and further limiting the accuracy of image reconstruction.

Data availability statement

All data that support the findings of this study are included within the article (and any supplementary files).

Acknowledgments

We thank Dr Takamiya Masanari (IBCS, KIT) for providing zebrafish samples.

Funding

This work was funded by the Helmholtz Association (Program Materials Science and Engineering), the Deutsche Forschungsgemeinschaft (DFG) through the Collaborative Research Center (CRC) 1324, the Karlsruhe School of Optics and Photonics (KSOP) and Research Training Group (RTG) 2039.

Conflict of interest

The authors declare no conflict of interest.

ORCID iD

Gerd Ulrich Nienhaus https://orcid.org/0000-0002-5027-3192

References

[1] Stelzer E H K, Strobl F, Chang B-J, Preusser F, Preibisch S and McDole K 2021 *Nat. Rev. Methods Primers.* **1** 73
[2] Keller P J, Schmidt A D, Wittbrodt J and Stelzer E H 2008 *Science* **322** 1065–9
[3] Chen B-C *et al* 2014 *Science* **346** 1257998
[4] Keller P J, Schmidt A D, Santella A, Khairy K, Bao Z, Wittbrodt J and Stelzer E H K 2010 *Nat. Methods* **7** 637–42
[5] Chang B-J, Kittisopikul M, Dean K M, Roudot P, Welf E S and Fiolka R 2019 *Nat. Methods* **16** 235–8
[6] Di Domenico G, Ruocco G, Colosi C, DelRe E and Antonacci G 2018 *Sci. Rep.* **8** 1–7
[7] Fahrbach F O, Gurchenkov V, Alessandri K, Nassoy P and Rohrbach A 2013 *Opt. Express* **21** 11425–40
[8] Remacha E, Friedrich L, Vermot J and Fahrbach F O 2020 *Biomed. Opt. Express* **11** 8–26
[9] Mohan K, Purnapatra S B and Mondal P P 2014 *PLoS One* **9** e96551
[10] Mazilu M, Stevenson D J, Gunn-Moore F and Dholakia K 2010 *Laser Photon. Rev.* **4** 529–47
[11] Ren Y-X, He H, Tang H and Wong K K Y 2021 *Front Phys.* **9** 698343
[12] Fahrbach F O, Simon P and Rohrbach A 2010 *Nat. Photon.* **4** 780–5
[13] Fahrbach F O and Rohrbach A 2012 *Nat. Commun.* **3** 632
[14] McGloin D and Dholakia K 2005 *Contemp. Phys.* **46** 15–28
[15] Baumgart E and Kubitscheck U 2012 *Opt. Express* **20** 21805–14
[16] Olarte O E, Andilla J, Gualda E J and Loza-Alvarez P 2018 *Adv. Opt. Photon.* **10** 111–79
[17] Preibisch S, Amat F, Stamataki E, Sarov M, Singer R H, Myers E and Tomancak P 2014 *Nat. Methods* **11** 645–8
[18] Schmid B and Huisken J 2015 *Bioinformatics* **31** 3398–400
[19] Hüpfel M, Merino M F, Bennemann J, Takamiya M, Rastegar S, Tursch A, Holstein T W and Nienhaus G U 2022 *Biomed. Opt. Express* **13** 147–58
[20] Chen B *et al* 2022 *Nat. Methods* **19** 1419–26
[21] Hüpfel M, Yu. Kobitski A, Zhang W and Nienhaus G U 2021 *Biomed. Opt. Express* **12** 969–80
[22] Chang B-J, Dean K M and Fiolka R 2020 *Opt. Express* **28** 27052–77
[23] Shi Y, Daugird T A and Legant W R 2022 *Nat. Commun.* **13** 4607
[24] Stockhausen A, Bürgers J, Rodriguez-Gatica J E, Schweihoff J, Merkel R, Prigge J M, Schwarz M K and Kubitscheck U 2020 *Opt. Express* **28** 15587–600
[25] Kimmel C B, Ballard W W, Kimmel S R, Ullmann B and Schilling T F 1995 *Dev. Dyn.* **203** 253–310
[26] Aleström P, D'Angelo L, Midtlyng P J, Schorderet D F, Schulte-Merker S, Sohm F and Warner S 2020 *Lab. Anim.* **54** 213–24
[27] Nienhaus K and Nienhaus G U 2017 Fluorescence labeling *Fluorescence Microscopy: From Principles to Biological Applications* ed U Kubitscheck (Wiley-VCH GmbH) pp 143–74
[28] Nienhaus K and Nienhaus G U 2022 *Methods Appl. Fluoresc.* **10** 042002
[29] Schindelin J *et al* 2012 *Nat. Methods* **9** 676–82
[30] Piedrahita-Quintero P, Castañeda R and Garcia-Sucerquia J 2015 *Appl. Opt.* **54** 6410–5
[31] Piedrahita-Quintero P and Garcia-Sucerquia J 2017 *Optik* **140** 626–33
[32] Ricci P, Gavryusev V, Müllenbroich C, Turrini L, de Vito G, Silvestri L, Sancataldo G and Pavone F S 2022 *Prog. Biophys. Mol. Biol.* **168** 52–65
[33] Fahrbach F O and Rohrbach A 2010 *Opt. Express* **18** 24229–44
[34] Antonacci G, Di Domenico G, Silvestri S, DelRe E and Ruocco G 2017 *Sci. Rep.* **7** 1–6
[35] Wan Y, McDole K and Keller P J 2019 *Annu. Rev. Cell. Dev. Biol.* **35** 655–81
[36] Chang B-J and Fiolka R 2019 *J. Phys. Photon.* **2** 014001
[37] Perez-Alvarez A, Huhn F, Durst C D, Franzelin A, Lamothe-Molina P J and Oertner T G 2021 *Front. Mol. Neurosci.* **14** 635820
[38] Cho E S, Han S, Lee K H, Kim C H and Yoon Y G 2021 *Opt. Express* **29** 32700–11
[39] Müllenbroich M C, Turrini L, Silvestri L, Alterini T, Gheisari A, Tiso N, Vanzi F, Sacconi L and Pavone F S 2018 *Front. Cell. Neurosci.* **12** 315
[40] Guo M *et al* 2020 *Nat. Biotechnol.* **38** 1337–46
[41] Liu G, Ruan X, Milkie D E, Görlitz F, Mueller M, Hercule W, Killilea A, Betzig E and Upadhyayula S 2023 *Sci. Adv.* **9** eade6623